Computers and Geotechnics 81 (2017) 87–97

Contents lists available at ScienceDirect

Computers and Geotechnics

journal homepage: www.elsevier.com/locate/compgeo

Technical Communication

A new approach for modeling landslide movement over 3D topography using 3D discontinuous deformation analysis

Wei Wang [b,c], Hong Zhang [a,*], Lu Zheng [d], Ying-bin Zhang [e,f], Yan-qiang Wu [g], Shu-guang Liu [a]

[a] College of Civil Engineering, Tongji University, Shanghai 200092, China
[b] Faculty of Engineering, China University of Geosciences (Wuhan), Wuhan 430074, China
[c] Department of Civil and Structural Engineering, Kyushu University, Fukuoka 819-0395, Japan
[d] The Hong Kong Polytechnic University, Institute for Disaster Management and Reconstruction, Sichuan University, Chengdu 610207, China
[e] Key Laboratory of Transportation Tunnel Engineering, Ministry of Education, Southwest Jiaotong University, Chengdu 610031, China
[f] Department of Geotechnical Engineering, School of Civil Engineering, Southwest Jiaotong University, Chengdu 610031, China
[g] First Crust Deformation Monitoring and Application Center, CEA, Tianjin 300180, China

ARTICLE INFO

Article history:
Received 1 January 2016
Received in revised form 25 July 2016
Accepted 30 July 2016

Keywords:
Landslide movement
3D topography
3D-DDA
Ordered blocky topography
Contact detection

ABSTRACT

Landslide movement analysis over three-dimensional (3D) topography is crucial for hazard evaluation and prevention. This paper presents a new approach to simulate landslide movement considering the 3D spatial effects of both the landslide mass and topography using discontinuous deformation analysis (DDA). The approach involves two aspects: the ordered blocky topography (OBT) treatment for the base slope and an algorithm for fast contact detection between the landslide block (LB) and the OBT. By introducing the OBT treatment, the LB-OBT contact detection can be simplified from the global range to the local sub-topography using the current algorithm, which enhances the computation efficiency. The approach has been implemented in the 3D-DDA program. Finally, the capability and performance of the proposed approach for landslide movement modeling were well demonstrated by two numerical examples.

1. Introduction

Landslides are considered among the most notable natural hazards around the world because of their frequent occurrence and catastrophic consequences. There have been many reports about landside-induced fatalities and economic losses, particularly along mountainous areas. For instance, more than 20,000 landslides were triggered by the 1999 Chi-Chi earthquake in Taiwan, causing more than 8000 causalities and nearly 10 billion US$ in economic losses [1–3]. Only a decade later, the 2008 Wenchuan earthquake shocked southwestern China and induced as many as 60,104 landslides, which consequently caused approximately 69,227 fatalities and destroyed innumerable infrastructures and houses [4–6]. The severe threats of landslides to people, property and environment depend largely on landslide velocity and travel distance, which are the main components of landslide movement [7]. Hence, the analysis of the post-failure behavior of a landside is of great importance to mitigation design and hazard evaluation and has drawn the attention of scholars worldwide.

Over the past few years, many methods have been proposed to analyze the post-failure movement of landslides based on the continuum mechanics. For example, Iverson et al. [7] employed a shock-capturing finite-volume method (FVM) and adaptive mesh refinement (AMR) to perform numerical simulation of a high-mobility landslide in Oso, Washington, USA. Similar simulation methods were also presented in previous studies [8–12]. In their simulation, the landslide mass was more likely treated as a continuous flow consisting of grain-fluid mixtures. Thus, they are very suitable for investigating the movement of rainfall-induced landslides with flow type. However, for landslides dominated by discontinuity, the continuous-based methods disregard the contact between individual rock masses, which causes difficulty in tracing the position or trajectory of the discrete rock mass during the landslide movement. In addition, with respect to the vertical information of the landslides in those simulations, only the landslide depth variation is presented while neglecting the vertical velocity information. Therefore, those simulations are not very useful for investigating landslide movement in three dimensions.

Regarding discrete numerical methods, the distinct element method (DEM) [13–17] and discontinuous deformation analysis (DDA) [18–25] are the most popular ones for modeling landslide

* Corresponding author.
E-mail address: hongzhang@tongji.edu.cn (H. Zhang).

http://dx.doi.org/10.1016/j.compgeo.2016.07.015
0266-352X/

movement and analyzing the deformation of mass bodies. Both DEM and DDA adopt the equations of dynamic motion, which are solved at finite points in a series of time steps, but there are some significant differences in their formulations of the solution scheme and contact mechanics [3]. In the solution scheme, the governing equations in DDA are derived by the principle of minimization of the total potential energy of the block system, similar to the finite element method (FEM), whereas the equations in DEM are obtained from the force balance. This implementation in DEM will result in unbalanced force after a certain computation step, so artificial damping is required to dissipate energy [26]. In the contact mechanics, DDA uses a penalty method in which the contact is assumed to be rigid. No overlapping or interpenetration is allowed, so the block system behaves like a real physical case. However, the soft contact approach used in DEM requires joint stiffness determined by laboratory test or field investigation, which may be difficult to obtain in many cases [3]. In summary, the DDA method has the advantages of both the DEM and FEM methods [27] and thus is very capable of analyzing landslide movement with large deformation and large displacement in a discontinuous blocky system.

Since the theory and numerical code of DDA were presented, many extensions and improvements to the original code have been proposed for a wide range of applications—for example, DDA simulation for seismic landslide movement [3,23,28,29] and rockfall analysis [18,30–32]. However, practical applications for landslides using DDA have concentrated thus far on the 2D problem. To extend to a more realistic practical problem, the 3D-DDA simulations are necessary for two reasons. First, the 3D spatial effects due to the rock fragment shape and topography are very important for the landslide movement in lateral directions. Second, the trees and barriers distributed in the 3D spatial could also affect the landslide movement.

Regarding the 3D-DDA method, only in recent years has a series of developments been achieved, having been first proposed in 2001 by Shi [20]. However, the development of 3D-DDA is still at an early stage, and most of the studies concentrate on the basic theory, especially the contact theory, because the contact mechanism between 3D blocks is rather complicated. To date, a set of contact models have been proposed to address the contact mechanism [24,27,33–42]. Particularly, Zhang et al. [24] presented a novel algorithm that can detect contacts between arbitrarily shaped 3D polyhedral blocks (both convex and concave blocks). Owing to these contributions, many test models employing simple geometries have been conducted to validate the performance and accuracy of 3D-DDA [43–45]. Nevertheless, the application for realistic landslide movement simulation is still very rare owing to the difficulties in topography implementation.

The purpose of this paper is to present a new approach for modeling landslide movement over complicated 3D topography using the 3D-DDA method. For this purpose, three problems should be addressed. The first is how to consider the topography in the computation. A proper method should then be developed to easily generate a complicated topography that can be incorporated in the block system for DDA simulation. The last point will be how to ensure the computational efficiency because more complicated topography indicates many more faces and vertices for contact detection. The details of the problems and their solutions could be found in the following sections.

2. Theory of 3D-DDA

In the DDA method, the formulation of blocks is very similar to that of finite element meshes. A problem is solved in which all elements are physically isolated blocks defined by preexisting discontinuities. The global equilibrium equations are derived by the principle of minimization of potential energy contributed by the noncontact and contact loadings. The large displacements are the accumulation of incremental displacements and deformations at each time step. Within each small time step, the incremental displacements of all points are relatively small, so the displacements can be reasonably represented by the first-order approximation.

2.1. Displacement and deformation

In the first-order approximation of displacement, it is assumed that each block has a constant strain and stress state in each time step. The displacements of an arbitrary point $P(x, y, z)$ in a 3D block i with centroid coordinates (x_c, y_c, z_c), $[u\ v\ w]^T$ are derived as follows [20]:

$$[u \quad v \quad w]^T = [\mathbf{T}_i(x,y,z)][\mathbf{D}_i] \tag{1}$$

$$[\mathbf{T}_i(x,y,z)] = \begin{bmatrix} 1 & 0 & 0 & 0 & Z & -Y & X & 0 & 0 & 0 & \frac{Z}{2} & \frac{Y}{2} \\ 0 & 1 & 0 & -Z & 0 & X & 0 & Y & 0 & \frac{Z}{2} & 0 & \frac{X}{2} \\ 0 & 0 & 1 & Y & -X & 0 & 0 & 0 & Z & \frac{Y}{2} & \frac{X}{2} & 0 \end{bmatrix} \tag{2}$$

$$[\mathbf{D}_i]^T = \begin{bmatrix} u_c & v_c & w_c & r_x & r_y & r_z & \varepsilon_x & \varepsilon_y & \varepsilon_z & \gamma_{yz} & \gamma_{zx} & \gamma_{xy} \end{bmatrix} \tag{3}$$

where $X = x - x_c$, $Y = y - y_c$, $Z = z - z_c$. $[\mathbf{T}_i(x, y, z)]$ is the displacement transformation matrix of the block at point $P(x, y, z)$. $[\mathbf{D}_i]$ indicates the vector of variables of the block center associated with the displacements and deformations, including rigid body translations (u_c, v_c, w_c), rigid body rotations (r_x, r_y, r_z), normal strain $(\varepsilon_x, \varepsilon_y, \varepsilon_z)$, and shear strains $(\gamma_{yz}, \gamma_{zx}, \gamma_{xy})$.

Error due to the approximation of using a linear displacement function causes block expansion, especially in problems involving large rigid body rotations [27]. Therefore, the post-correction of the displacement of point $P(x, y, z)$ is applied after each step as

$$[u \quad v \quad w]^T = [\mathbf{T}_i(x,y,z)][\mathbf{D}_i] - \begin{bmatrix} 0 & Z & -Y \\ -Z & 0 & X \\ Y & -X & 0 \end{bmatrix} \begin{bmatrix} r_x \\ r_y \\ r_z \end{bmatrix} + \begin{bmatrix} \cos r_y + \cos r_z - 2 & -\sin r_z & \sin r_y \\ \sin r_z & \cos r_z + \cos r_x - 2 & -\sin r_x \\ -\sin r_y & \sin r_x & \cos r_x + \cos r_y - 2 \end{bmatrix} \begin{bmatrix} X \\ Y \\ Z \end{bmatrix} \tag{4}$$

Because the displacement function is a linear function of coordinates (x, y, z), the 3D integration of 3D blocks for 3D-DDA are of degree 0, 1, 2. The volume of 3D blocks can then be computed by the 3D simplex integration [20]. Using the 3D simplex integration, the volume of a block with complex geometry (convex for concave polyhedral) can be easily calculated without dividing it into small blocks [46,47].

2.2. Governing equations

DDA is a Lagrangian work-energy-based method, the formulation of which is derived using the principle of minimum total potential energy. The summation of the potential energy contributed by: (1) the elastic stress, (2) the initial constant stresses, (3) the body forces, (4) the point loading, (5) the inertia forces, (6) the constraint spring of fixed points and (7) contact forces of the block system should be minimized at each computation step. By applying the principle, the equilibrium equations are assembled by all of the terms of the differentiations of the n block system as

$$\begin{bmatrix} [\mathbf{K}_{11}] & [\mathbf{K}_{12}] & \cdots & [\mathbf{K}_{1n}] \\ [\mathbf{K}_{21}] & [\mathbf{K}_{22}] & \cdots & [\mathbf{K}_{2n}] \\ \vdots & \vdots & \vdots & \vdots \\ [\mathbf{K}_{n1}] & [\mathbf{K}_{n2}] & \cdots & [\mathbf{K}_{nn}] \end{bmatrix} \cdot \begin{bmatrix} [\mathbf{D}_1] \\ [\mathbf{D}_2] \\ \vdots \\ [\mathbf{D}_n] \end{bmatrix} = \begin{bmatrix} [\mathbf{F}_1] \\ [\mathbf{F}_2] \\ \vdots \\ [\mathbf{F}_n] \end{bmatrix} \tag{5}$$

Because each block i has 12 degrees of freedom, $[\mathbf{K}_{ii}]$ is a 12×12 stiffness sub-matrix depending on the material properties of block i, and $[\mathbf{K}_{ij}]$ ($i \neq j$) is defined by the contacts between blocks i and j. $[\mathbf{D}_i]$ and $[\mathbf{F}_i]$ are 12×1 displacement and loading submatrices of block i, respectively. The final displacement variables for a given time step are actually obtained by solving Eq. (5) iteratively until no tension of penetration is found over all contacts, which is well known as "open-close" iteration [19].

2.3. Contact mechanism

Any block in 3D can be presented by a set of boundary vertices, edges and polygons. The contact between the blocks in the blocky system can occur only at their boundaries. Therefore, the contact can be categorized into seven types, including vertex-to-vertex (V-V), vertex-to-edge (V-E), vertex-to-face (V-F), crossing edge-to-edge (E-E), parallel edge-to-edge (E-E), edge-to-face (E-F), and face-to-face (F-F). However, only the first four type of contacts are examined during the contact detection, because the other three types of contacts can be treated as combinations of the four basic types [24,26]. As illustrated in Fig. 1, an F-F contact is examined between block i and block j. It is then converted into four basic contacts—i.e., $C1$ (V-V), $C2$ (V-E), $C3$ (V-F), and $C4$ (E-E).

After determining the contact type, the entrance mode to define the entrance plane (EP) of the contact will be assigned to each contact. In 3D-DDA, there are two types of entrance modes: point-to-plane entrance (P-P) and crossing line-to-line entrance (L-L). For the V-F contact, there is only one EP, which is defined by the P-P entrance. For the crossing E-E contact shown in Fig. 2, the entrance mode can also be directly termed as the L-L entrance, and only one EP exists. In terms of V-E and V-V contacts, there will be multiple entrances modes and EPs. Regarding the details of the contact mechanism between polyhedral blocks in 3D, readers can refer to the fundamental study presented by Zhang et al. [24].

After the determination of the entrance plane based on the entrance mode, the subsequent contact force can be calculated. In the DDA method, the penalty technique is used to prevent inter-penetration between blocks. When two blocks make contact with each other and penetration occurs, a deformed spring can be added in normal or/and sliding direction(s) to avoid penetration. The spring force magnitude is calculated according to the penetration distance. In fact, at each time step, adding or removing a spring (open-close iteration) is used to satisfy no-tension, no-penetration conditions for every contact before proceeding to the next time step. In the DDA method, the contact state between blocks has three types: *locked*, *sliding* and *open*. The contact state is determined by the Mohr–Coulomb failure criterion as follows:

if $k_n d_n > 0$, and $k_s d_s \leqslant k_n d_n \tan\varphi + cA \rightarrow$ *locked*;

if $k_n d_n > 0$, and $k_s d_s > k_n d_n \tan\varphi + cA \rightarrow$ *sliding*;

if $k_n d_n < 0 \rightarrow$ *open*.

where d_n and d_s are the penetration distance in the normal and shear directions, respectively. k_n and k_s are the stiffness of the normal and shear spring, respectively. c (cohesion) and φ (friction angle) are the strength parameters of the joint, and A is the contact area. For the *open* state, there is no normal or shear spring added between the contacts. In contrast, both the normal and shear springs will be added between *locked* contacts. A pair of frictional springs and a normal spring will be added on a sliding contact. Fig. 3 shows the disposal of the *sliding* state for a V-F contact.

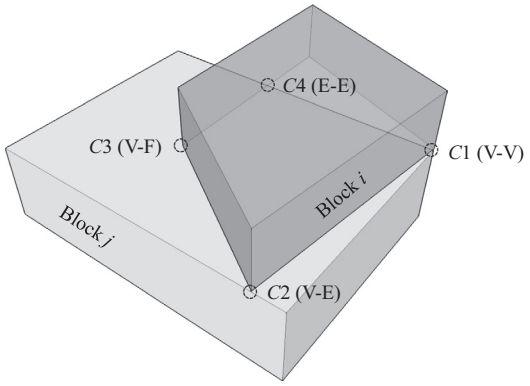

Fig. 1. Schematic view of the combination of four basic contacts for a F-F contact.

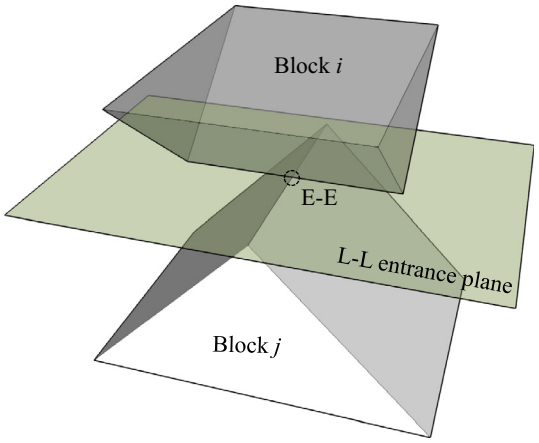

Fig. 2. Illustration of an L-L entrance plane for a crossing E-E contact.

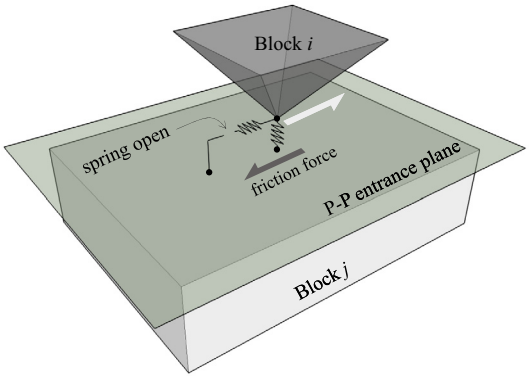

Fig. 3. Disposal of a V-F contact with *sliding* state.

3. Treatment of the topography

For the simulation of landslide movement over 3D topography, a very large base area is required, which should include the source area, slope and potential run-out area. In the original 2D-DDA, the base of the slope or named topography is treated as a single block. By this treatment, the original 2D-DDA can be extended for more practical engineering problems.

Regarding the treatment of topography in 3D-DDA, very few works on this problem have been published. A possible solution for the problem is to introduce the topography as the contact face element (CFE) in 3D-DDA [18,48]. In this treatment, the surface of the topography is discretized as a series of ordered contact faces that function as the boundary constraint for the falling blocks. The CFE implementation for the topography takes advantage of ordered contact faces, so it greatly improves the efficiency of the contact detection between the base slope and landslide blocks. However, in the CFE implementation, the contact between the landslide blocks and topography has only two types, V-F and E-E, which is not sufficient compared with the four basic contact types in the current study.

If the topography is treated as a single block, it is able to develop more extensions for practical engineering using 3D-DDA, especially for the movement modeling of seismic landslides. Furthermore, the previously introduced improved contact mechanism (Section 2.3) can be naturally inherited for the contact detection process between the landslide blocks and topography block. Nevertheless, computational complexity can arise during the calculation, because a vast number of faces is always required for the topography block to present the 3D terrain. In this case, numerous iterations of detection for potential contact will be consumed even between one landslide block and the topography. As a result, the computation efficiency will decrease, especially for a practical case involving many blocks.

In summary, both the CFE and single block treatments for the topography have their own merits and limitations. To ensure extensibility and computational efficiency, we consider the topography as a single block in which the upper surface is made up of a series of ordered triangle faces as that in the CFE implementation.

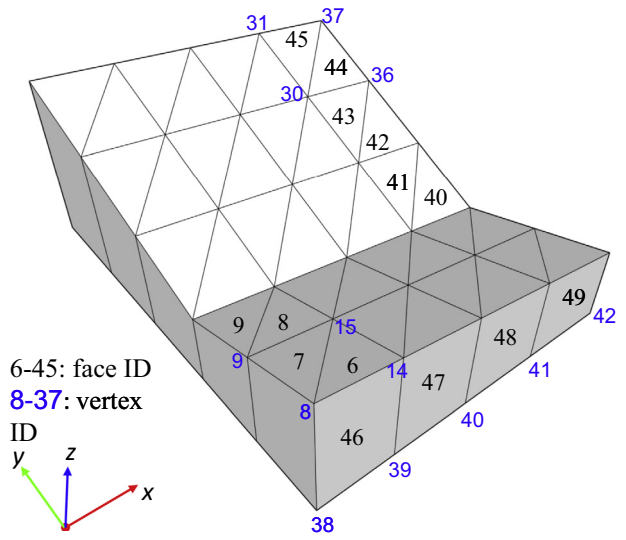

Fig. 4. Illustration of a simple OBT model.

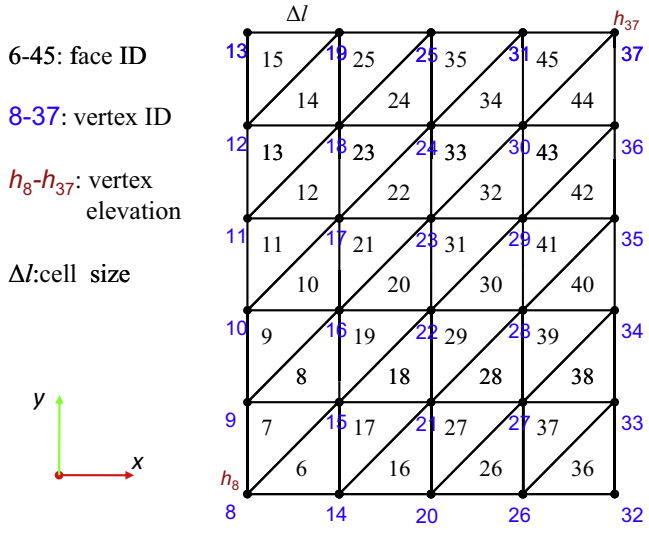

Fig. 5. Projection view of the upper surface of the OBT.

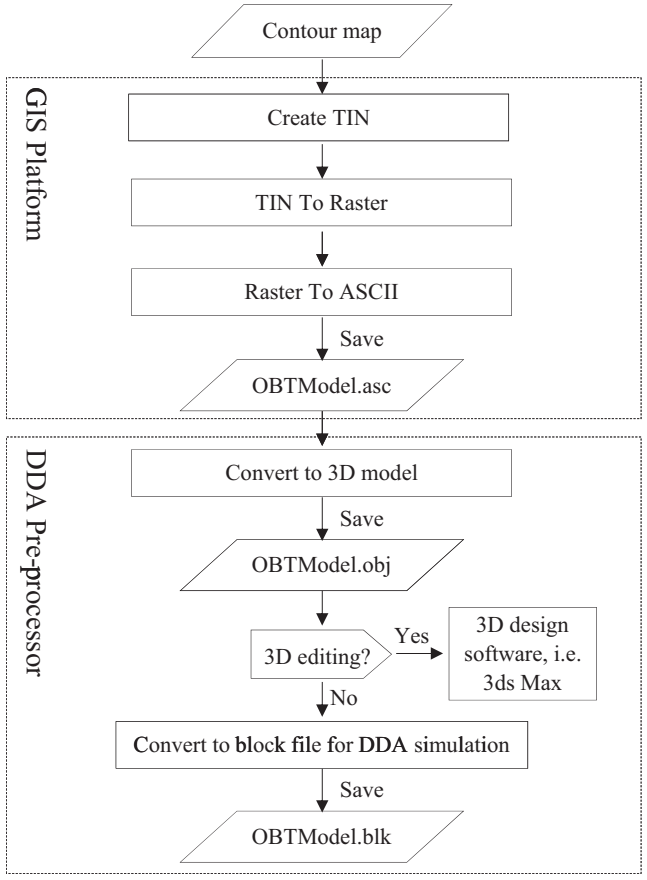

Fig. 6. Process flow to generate an OBT model using the GIS platform and the DDA pre-processor.

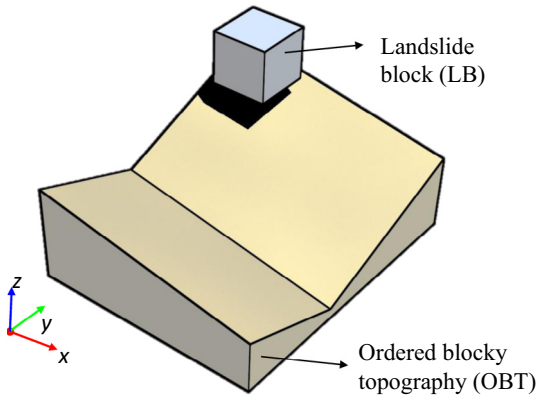

Fig. 7. An example that a block (LB) falls down to a base block (OBT).

The proposed new treatment is named ordered blocky topography (OBT), which combines the merits of both the CFE and single block treatments. The advantages of the OBT are the following:

1. It is easy to implement the contact detection algorithm between the landslide blocks (LB) and OBT because the regular faces in the upper surface are arranged orderly.
2. The computation efficiency can be largely enhanced by the implementation of the fast contact detection algorithm.
3. The contact mechanism can be naturally inherited during the contact detection process between the LB and OBT without any special treatment.

4. Ordered blocky topography

4.1. Overview

The main feature of the OBT is that the upper surface consists of a series of regular triangular faces that are arranged orderly. Fig. 4 shows a simple OBT model. In this model, the upper surface of the OBT is made up of 30 vertices ranging from 8 to 37, and 40 faces numbered from 6 to 45.

To present the features of the OBT in detail, the projection view of the upper surface in the *xy* plane is presented in Fig. 5. Apparently, the surface is first decomposed into 5 rows and 4 columns, totaling 20 cells and 30 vertices. Each vertex of the upper surface is continuously numbered and given a certain elevation (z value) to form the 3D topography shown in Fig. 4. Moreover, each cell has a size of Δl and is divided into 2 basic triangles. Finally, the upper surface has a total number of 40 basic triangles continuously numbered in the y direction. Therefore, the data structure of the vertices and faces of the OBT is rigorously ordered, which will benefit the contact detection between the LB and OBT.

4.2. Model generation

To simulate the landslide movement over a 3D topography using OBT, a proper method should be developed to easily generate the OBT model in the first step. Considering the features of the OBT introduced in Section 4.2, the data structure is analogous to the ASCII raster data in ArcGIS. In addition, it is very convenient to address any complicated topography data using the GIS platform because of its robust abilities in working with maps and geographic information. Therefore, it is possible to generate an OBT model originating from raw topography data such as a contour map using the GIS platform.

Fig. 6 shows the process flow of the means by which to generate an OBT model from a contour map. Providing a contour map of the

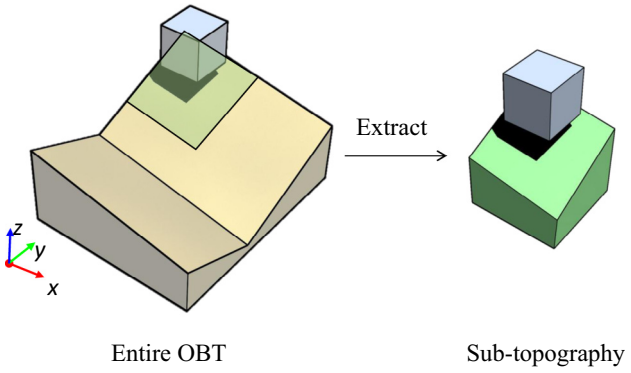

Fig. 9. Key idea of the algorithm for LB-OBT contact detection.

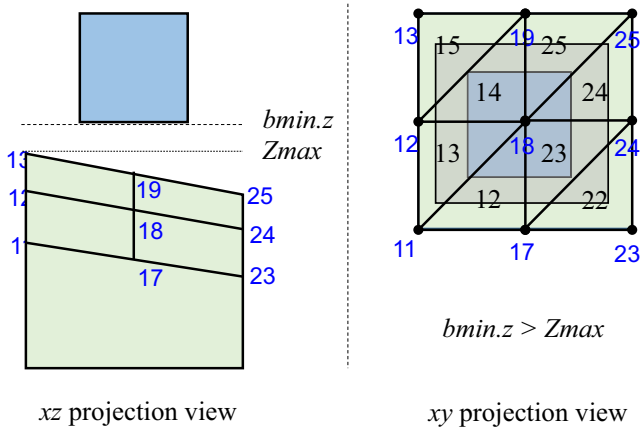

Fig. 10. No contact will be detected if *bmin·z* > *Zmax*.

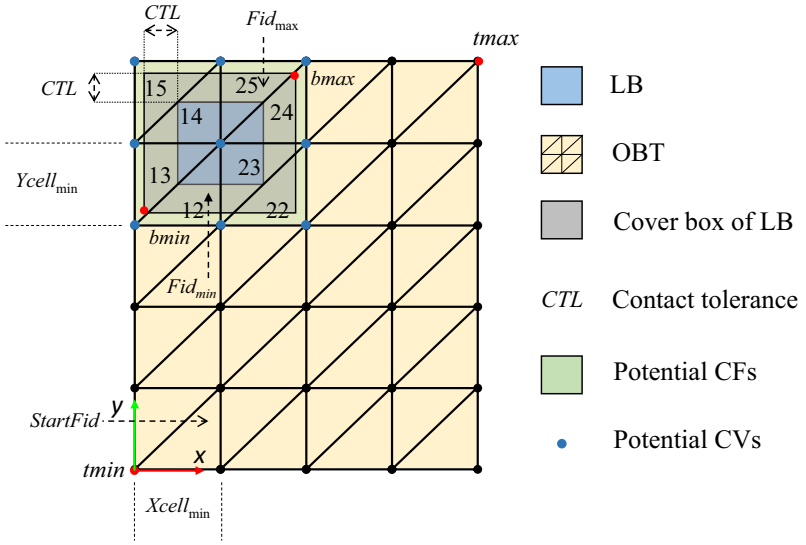

Fig. 8. *xy* projection view of the example model. *tmin* and *tmax* is the minimum and maximum bound point of the OBT; *bmin* and *bmax* is the minimum and maximum bound point of the LB; $Xcell_{min}$ and $Ycell_{min}$ is the column ID and row ID of the cell where *bmin* in; *StartFid* indicates the index of the first triangle face of the OBT; Fid_{min} and Fid_{max} denote the index of the triangle face where *bmin* and *bmax* in, respectively.

topography, the ASCII raster data (OBTModel.asc) of the topography can be obtained using a series of 3D analytical operations in the GIS platform. The ASCII raster data file will then be converted into a formatted file (OBTModel.obj) representing the 3D geometry of the OBT by the DDA pre-processor. The OBJ file format is a simple data format adopted by many 3D design applications so that the OBT can be visualized and edited easily by making use of software such as the 3ds Max. Finally, the OBJ file of the OBT will be converted to a block file (OBTModel.blk) that can be processed in the next DDA simulation.

4.3. LB-OBT contact detection

Owing to the ordered structure of the faces and vertices in the OBT, an efficient search algorithm can be implemented to detect the potential contact faces and vertices between the LB and OBT. To explain the search algorithm for the LB-OBT contact detection, Fig. 7 shows a simple example in which an upper block (hereinafter referred as LB) falls down to a base block (hereinafter referred as OBT). Fig. 8 shows the *xy* projection view of the model, in which the projection of the LB is located in the upper-right corner of the projection of OBT.

The first step of the LB-OBT contact detection is to search for the potential contact faces (CFs) of the OBT. Denote $x_{\min}$, $y_{\min}$, $x_{\max}$, and $y_{\max}$ as the coordinates of the minimum and maximum bound points of the LB in the projection view. The potential CFs can be restricted in the cover box of the LB defined by the minimum bound point (*bmin*) and maximum bound point (*bmax*), respectively. The bound points of the cover box are enlarged from the bound points of the LB by a contact tolerance (*CTL*) and can be expressed by

$$\left.\begin{aligned} bmin\cdot x &= x_{min} - CTL \\ bmin\cdot y &= y_{min} - CTL \\ bmax\cdot x &= x_{max} + CTL \\ bmax\cdot y &= y_{max} + CTL \end{aligned}\right\} \tag{6}$$

Furthermore, if the bound points of the cover box in Fig. 8 are out of the extent of the OBT, the coordinates of these points will be adjusted. Denote *tmin* and *tmax* as the minimum and maximum bound points of the OBT; the adjustment is described as

$$\left.\begin{aligned} bmin\cdot x &= max(bmin\cdot x, tmin\cdot x) \\ bmin\cdot y &= max(bmin\cdot y, tmin\cdot y) \\ bmax\cdot x &= min(bmax\cdot x, tmax\cdot x) \\ bmax\cdot y &= min(bmax\cdot y, tmax\cdot y) \end{aligned}\right\} \tag{7}$$

Because the projection of the OBT has a fixed number of regular rows and columns, the cell index ($Xcell_{\min}$, $Ycell_{\min}$, $Xcell_{\max}$, $Ycell_{\max}$) of the point *bmin* and *bmax* can be directly calculated by

$$\left.\begin{aligned} Xcell_{\min} &= \mathrm{int}\left(\tfrac{bmin\cdot x - tmin\cdot x + \Delta l}{\Delta l}\right) \\ Ycell_{\min} &= \mathrm{int}\left(\tfrac{bmin\cdot y - tmin\cdot y + \Delta l}{\Delta l}\right) \\ Xcell_{\max} &= \mathrm{int}\left(\tfrac{bmax\cdot x - tmin\cdot x + \Delta l}{\Delta l}\right) \\ Ycell_{\max} &= \mathrm{int}\left(\tfrac{bmax\cdot y - tmin\cdot y + \Delta l}{\Delta l}\right) \end{aligned}\right\} \tag{8}$$

where *tmin* is the origin of the OBT in the projection view; Δl is the cell size; and operation "int()" indicates integer conversion. It should be noted that the basic face of the upper surface in an OBT is the triangle, and each cell is divided into 2 such triangles. Therefore, the minimum and maximum indexes of the potential CFs ($Fid_{\min}$, $Fid_{\max}$) can be determined by

$$\left.\begin{aligned} Fid_{\min} &= StartFid + 2(Ycnt(Xcell_{\min} - 1) + Ycell_{\min}) - 2 \\ Fid_{\max} &= StartFid + 2(Ycnt(Xcell_{\max} - 1) + Ycell_{\max}) - 1 \end{aligned}\right\} \tag{9}$$

where *StartFid* is the index of the first triangle of the OBT; *Ycnt* indicates the number of cells in one column. Through this procedure,

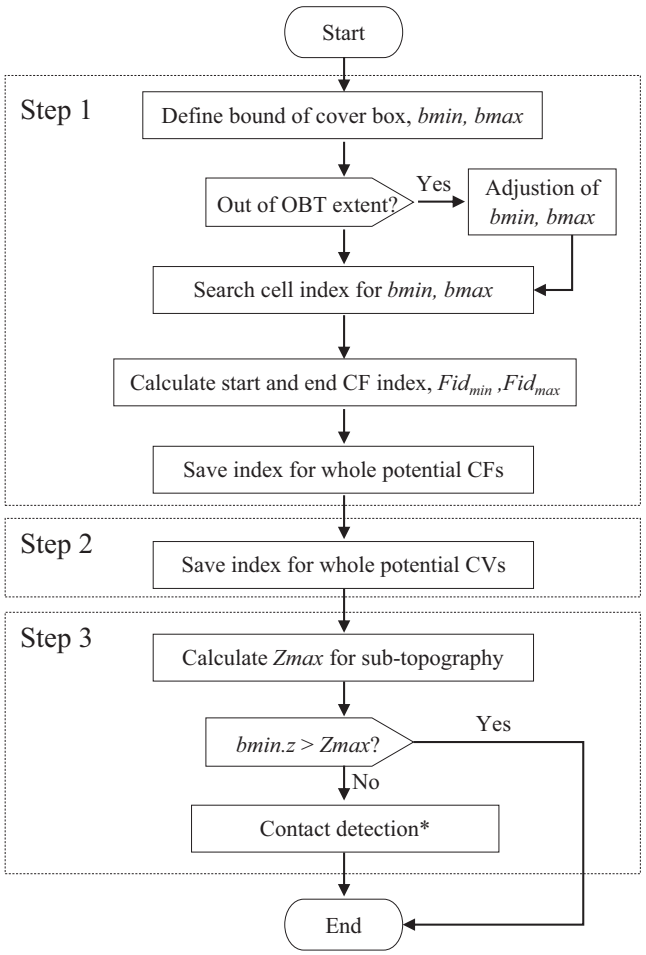

Fig. 11. Process flow for the LB-OBT contact detection. Details of the process "*" can be found in Zhang et al. [24].

$Fid_{\min}$ and $Fid_{\max}$ of the illustrated model are defined as 12 and 25, respectively. Based on this, the calculation of the index of all potential CFs (12–15, 22–25) can be programmed as

```
int fcnt;  //count of potential CFs
int* fid;  //index of whole CFs
icnt=xcellmax-xcellmin+1;  //count of potential
  cells in x direction
jcnt=ycellmax-ycellmin+1;
fcnt=0;
for (int i=0; i<icnt; i++)
{
  for (int j=0; j<jcnt*2; j++)
  {
    fid[fcnt]=fidmin+i*lO+j;
    fcnt++;
  }
}
```

The second step of the LB-OBT contact detection is to search for the potential contact vertices (CVs) of the OBT. In the same manner, the index of the potential CVs of the illustrated model can also be determined as shown in Fig. 8 (i.e., vertex in blue[1] dots in the current

[1] For interpretation of color in Fig. 8, the reader is referred to the web version of this article.

model). In fact, the key idea of the algorithm for the LB-OBT contact detection is to extract the sub-topography from the entire OBT that can potentially interacts with the upper LB, shown in Fig. 9.

In addition, it should be noted that when the minimum Z coordinate ($bmin{\cdot}z$) of the cover box of the LB is beyond the maximum elevation of the sub-topography ($Zmax$), the contact detection between the LB and OBT can be skipped. As shown in Fig. 10, it is impossible for the LB to make contact with the sub-topography even if the xy projection of the LB is included in the sub-topography.

In summary, the process flow of the LB-OBT contact detection can be presented in Fig. 11. "$*$" indicates the last operation in step 3, which was clarified in detail by Zhang et al. [24]. By implementing the algorithm for LB-OBT contact detection, the potential CFs and CVs can be detected quickly, which greatly accelerates the computational efficiency. After the contact detection, the OBT is excluded from solving the global equilibrium equation (5). In the proposed approach, the OBT acts as the bottom boundary of the LB, whereas the sub-matrices of the contact terms (i.e. normal spring force, shear spring force, frictional force) for the landslide blocks are still assembled into the global stiffness matrix. By this treatment, the convergence of the time stepping in the open-close iterations due to large differences in size is ensured, and the improved contact algorithm between the landslide block and base block can be naturally inherited.

Table 1
Material properties and control parameters in the simple model test.

Description	Notation	Value
Density	ρ (kg/m^3)	2000
Elastic modulus	E (GPa)	1.0
Poisson's ratio	υ	0.3
Cohesion of discontinuities	c (MPa)	0
Friction angle of discontinuities	φ (°)	10
Gravity acceleration	g (m/s^2)	−9.8
Contact spring stiffness	k (kN/m)	10^6
Time interval	Δt (s)	0.0005
Total time steps	N	5600

5. Numerical examples

To validate the capability and performance of the proposed approach for modeling the landslide movement over 3D topography, two numerical examples were carried out. The first one employs a simple model introduced in Section 4.3, and the second example shows the landslide movements over complicated 3D topography.

5.1. Simple model test

As depicted in Fig. 7, the simple model consists of 2 blocks, a base block and a falling block. The base block is treated as the OBT with 40 basic triangles forming the upper surface. The cell size of the OBT is 1 m, and the falling block is a 1 m × 1 m × 1 m cube. The falling block is initially placed slightly beyond the upper-left corner of the base block. The material properties and control parameters for the test are illustrated in Table 1.

Fig. 12 shows the photo sequences of the simulation. It can be seen in the simulation result that the falling block moves along one side of the slope in the first 1.1 s. Subsequently, the falling

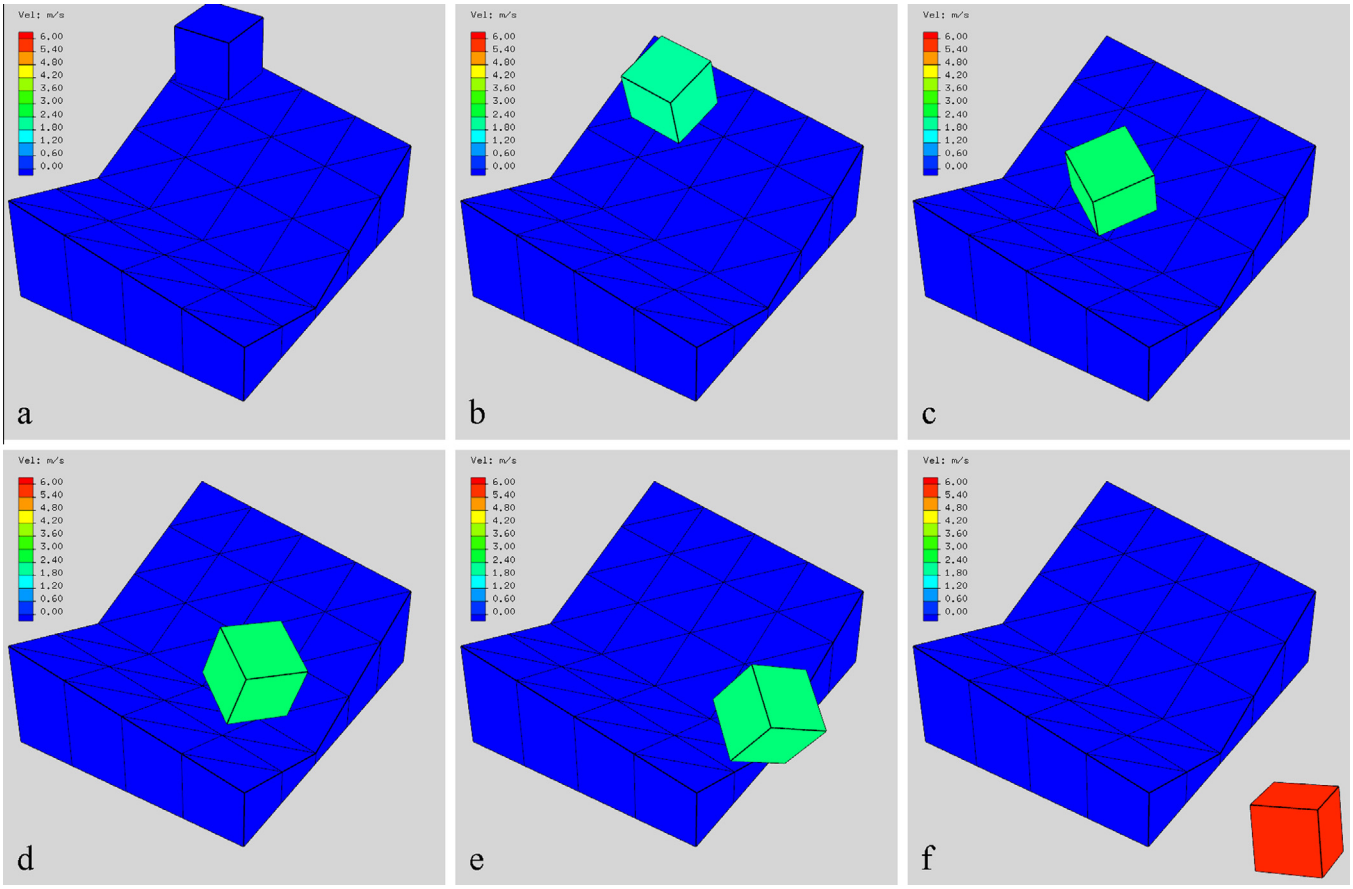

Fig. 12. Simulation sequences of the simple model test. (a) t = 0 s; (b) t = 0.5 s; (c) t = 1.1 s; (d) t = 1.7 s; (e) t = 2.2 s; (f) t = 2.8 s.

block reaches the bottom of the base block and interacts with the other side of the slope. Finally, the falling block moves out of the base block and starts a free-fall. Apparently, the interaction between the falling block (LB) and the base block (OBT) is well presented during the whole process using the proposed approach. In addition, the topography and 3D effect of the block geometry can be well demonstrated by the 3D-DDA method.

5.2. Landslide with complicated topography

In order to demonstrate the performance and applicability of the proposed method in dealing with the landslide movement over complicated 3D topography, the numerical example in this section employs a slope with rather complex terrain. In this case, the slope has a length of 650 m, and width of 390 m. The generation process of the OBT model for the base block is presented by a sequence of pictures shown in Fig. 13.

The landslide mass has a length of 50 m, average width of 40 m, and average depth of 22 m. The landslide mass consists of 36 LBs, with a volume approximate 44,000 m^3 in total. The material properties and control parameters for the movement simulation are given in Table 2. The total time of the simulation is approximate 26 s with more than 132,000 steps, which takes about 3 h on a Windows device with an Intel Core(TM) i7 CPU (3.60 GHz) and a 24 Gb RAM.

Fig. 14 presents the typical simulation instance of the landslide movement over the complicated 3D topography. The simulated results show that the initiation of the sliding occurs in the first 4 s. Soon thereafter, most of the landslide blocks are sliding along the slope, while a few blocks remain on the upper slope (Fig. 14c and d). Subsequently, the landslide mass travels to the foot of the slope, and many of the blocks are stopped by the slight rise in the topography. In general, the landslide movement in the 3D space coincides well with the local topography.

In this numerical example, blocks with relative regular size and shapes were generated to present the landside mass. In general, the size and shape of the blocks may have influence on the numerical stability and convergence. There are two major reasons to explain this problem. First, the complexity of the block shape may arise difficulties in determining the entrance plane of the contact. Second, large difference in size may result in interpenetrations, such as the problem of very small edge. Shi recently [36,37] published a new contact theory to deal with this problem. It is expected to significantly facilitate the contact treatment after the code is totally completed and successfully implemented in the current program.

Table 2
Material properties and control parameters for the simulation with complicated 3D topography.

Description	Notation	Value
Density	ρ (kg/m^3)	2500
Elastic modulus	E (GPa)	5.0
Poisson's ratio	υ	0.3
Cohesion of discontinuities	c (MPa)	0
Friction angle of discontinuities	φ (°)	15
Gravity acceleration	g (m/s^2)	−9.8
Contact spring stiffness	k (kN/m)	2.0×10^7
Time interval	Δt (s)	0.0002
Total time steps	N	132,000

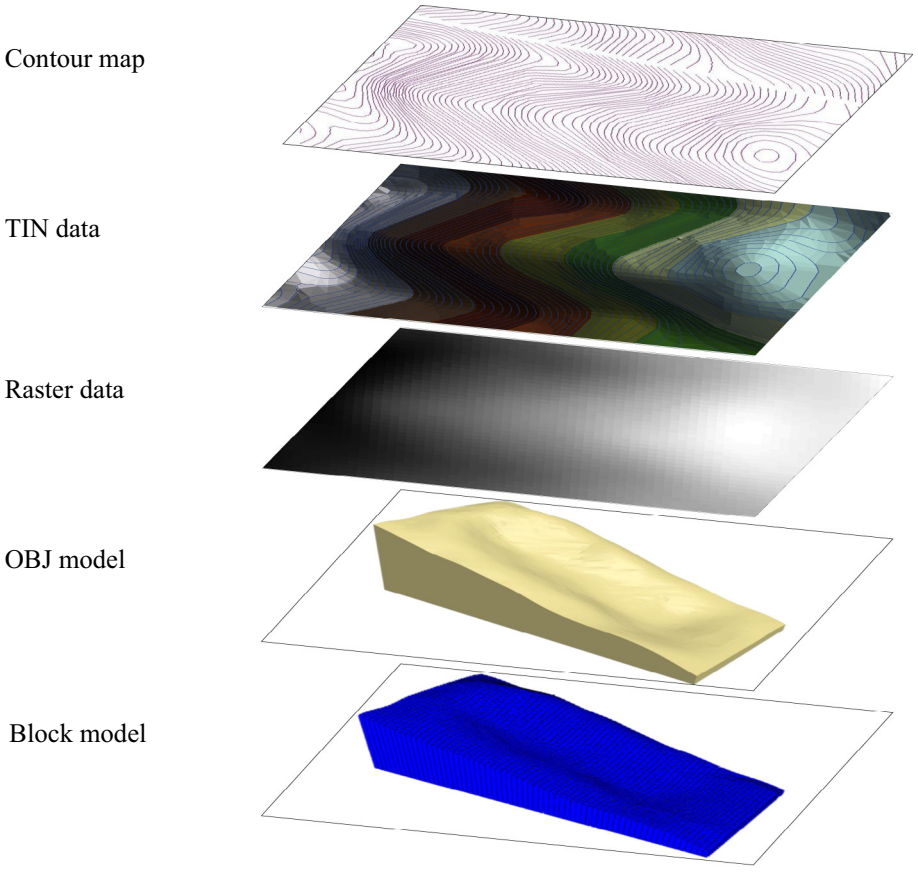

Fig. 13. Model generation process of the OBT for the base block with complicated topography.

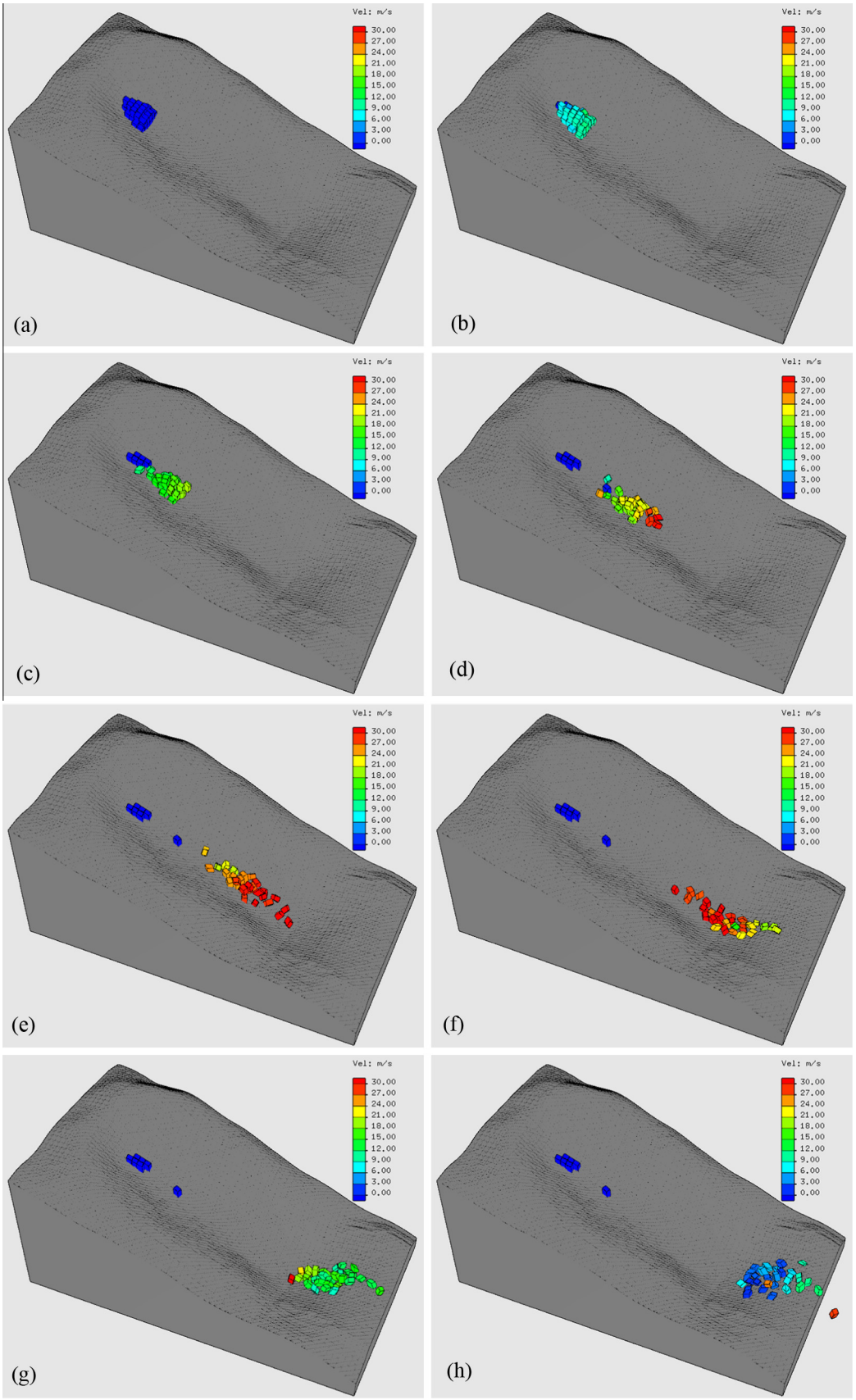

Fig. 14. Simulation sequences of the landslide movement over complicated 3D topography. (a) $t = 0$ s; (b) $t = 4.0$ s; (c) $t = 8.0$ s; (d) $t = 12.0$ s; (e) $t = 14.0$ s; (f) $t = 20.0$ s; (g) $t = 23.2$ s; (h) $t = 26.3$ s.

6. Conclusions

Three-dimensional simulation of landslide movement over complicated topography is very important for hazard evaluation and mitigation design in practical engineering. For this purpose, we proposed a new approach involving the OBT treatment and contact detection algorithm between the OBT and LB.

By introducing the OBT, LB-OBT contact detection can be simplified from the global topography to the local sub-topography, which enhances the computation efficiency. The generation method of the OBT was also well clarified. The new approach was then implemented in the 3D-DDA code, and two numerical examples were carried out for the performance and capability evaluation.

In the simple model test, the interaction between the falling block (LB) and the base block (OBT) is well presented during the whole process using the proposed approach. In the second example, the landslide (LB) movement in the 3D space coincides well with the local topography (OBT), which demonstrates the applicability and performance of the proposed approach in dealing with the landslide movement over 3D topography.

Although a reliable approach has been proposed to fulfill the 3D simulation of landslide movement over complicated topography in this study, there still remain some issues to be addressed in the future. For instance, in the model generation, a proper method should be developed to cut the landslide blocks directly from the topography block. In addition, the current code of 3D-DDA should be applied for more complicated, realistic cases, such as those with a large number of blocks. Nevertheless, the approach in this study is believed to provide a solid foundation for landslide movement analysis for practical engineering cases.

Acknowledgement

The authors extend their gratitude to three anonymous reviewers for their insightful comments. In addition, the authors appreciate the financial support from National Science & Technology Pillar Program of the Ministry of Science and Technology of China (Grant No. 2014BAL05B01).

References

[1] Chang K-J, Taboada A, Lin M-L, Chen R-F. Analysis of landsliding by earthquake shaking using a block-on-slope thermo-mechanical model: example of Jiufengershan landslide, central Taiwan. Eng Geol 2005;80(1):151–63.
[2] Togo T, Shimamoto T, Dong JJ, Lee CT, Yang CM. Triggering and runaway processes of catastrophic Tsaoling landslide induced by the 1999 Taiwan Chi-Chi earthquake, as revealed by high-velocity friction experiments. Geophys Res Lett 2014;41(6):1907–15.
[3] Zhang Y, Chen G, Zheng L, Li Y, Wu J. Effects of near-fault seismic loadings on run-out of large-scale landslide: a case study. Eng Geol 2013;166:216–36.
[4] Dai F, Xu C, Yao X, Xu L, Tu X, Gong Q. Spatial distribution of landslides triggered by the 2008 Ms 8.0 Wenchuan earthquake, China. J Asian Earth Sci 2011;40(4):883–95.
[5] Gorum T, Fan X, van Westen CJ, Huang RQ, Xu Q, Tang C, et al. Distribution pattern of earthquake-induced landslides triggered by the 12 May 2008 Wenchuan earthquake. Geomorphology 2011;133(3):152–67.
[6] Xu C, Xu X, Yao X, Dai F. Three (nearly) complete inventories of landslides triggered by the May 12, 2008 Wenchuan Mw 7.9 earthquake of China and their spatial distribution statistical analysis. Landslides 2014;11(3):441–61.
[7] Iverson RM, George DL, Allstadt K, Reid ME, Collins B, Vallance JW, et al. Landslide mobility and hazards: implications of the 2014 Oso disaster. Earth Planet Sci Lett 2015;412:197–208.
[8] Cascini L, Cuomo S, Pastor M. Inception of debris avalanches: remarks on geomechanical modelling. Landslides 2013;10(6):701–11.
[9] Cascini L, Cuomo S, Pastor M, Sorbino G, Piciullo L. SPH run-out modelling of channelised landslides of the flow type. Geomorphology 2014;214:502–13.
[10] Iverson R, George D. Modelling landslide liquefaction, mobility bifurcation and the dynamics of the 2014 Oso disaster. Géotechnique 2014;2015:1–13.
[11] Kuo Y-S, Tsai Y-J, Chen Y-S, Shieh C-L, Miyamoto K, Itoh T. Movement of deep-seated rainfall-induced landslide at Hsiaolin Village during Typhoon Morakot. Landslides 2013;10(2):191–202.
[12] Pastor M, Blanc T, Haddad B, Petrone S, Morles MS, Drempetic V, et al. Application of a SPH depth-integrated model to landslide run-out analysis. Landslides 2014;11(5):793–812.
[13] Cundall PA, Strack O. The development of constitutive laws for soil using the distinct element method. Numer Meth Geomech 1979;1:289–317.
[14] Hart R. General report: an introduction to distinct element modelling for rock engineering. In: 7th ISRM congress. Aachen, Germany: International Society for Rock Mechanics; 1991.
[15] Hungr O, Corominas J, Eberhardt E. Estimating landslide motion mechanism, travel distance and velocity. Landslide Risk Manage 2005:99–128.
[16] Kveldsvik V, Kaynia AM, Nadim F, Bhasin R, Nilsen B, Einstein HH. Dynamic distinct-element analysis of the 800m high Åknes rock slope. Int J Rock Mech Min Sci 2009;46(4):686–98.
[17] Tang C-L, Hu J-C, Lin M-L, Angelier J, Lu C-Y, Chan Y-C, et al. The Tsaoling landslide triggered by the Chi-Chi earthquake, Taiwan: insights from a discrete element simulation. Eng Geol 2009;106(1):1–19.
[18] Chen G, Zheng L, Zhang Y, Wu J. Numerical simulation in rockfall analysis: a close comparison of 2-D and 3-D DDA. Rock Mech Rock Eng 2013;46(3):527–41.
[19] Shi GH. Discontinuous deformation analysis: a new numerical model for the statics and dynamics of block systems [Ph.D. thesis]. Berkeley: University of California; 1988.
[20] Shi GH. Three dimensional discontinuous deformation analysis. In: Proceedings of the fourth international conference on analysis of discontinuous deformation, Scotland; 6–8 June 2001. p. 1–21.
[21] Shi G-H, Goodman RE. Discontinuous deformation analysis. In: Proceedings of 25th U.S. symposium on rock mechanics. Evanston (IL), USA: SME/AIME; 1984. p. 269–77.
[22] Wang W, Chen G, Zhang H, Zhou S, Liu S, Wu Y, et al. Analysis of landslide-generated impulsive waves using a coupled DDA-SPH method. Eng Anal Boundary Elem 2016;64:267–77.
[23] Wu J-H, Chen C-H. Application of DDA to simulate characteristics of the Tsaoling landslide. Comput Geotech 2011;38(5):741–50.
[24] Zhang H, Chen G, Zheng L, Han Z, Zhang Y, Wu Y, et al. Detection of contacts between three-dimensional polyhedral blocks for discontinuous deformation analysis. Int J Rock Mech Min Sci 2015;78:57–73.
[25] Zhang Y, Xu Q, Chen G, Zhao JX, Zheng L. Extension of discontinuous deformation analysis and application in cohesive-frictional slope analysis. Int J Rock Mech Min Sci 2014;70:533–45.
[26] Cundall PA, Hart RD. Numerical modelling of discontinua. Eng Comput 1992;9(2):101–13.
[27] Jiang Q, Yeung M. A model of point-to-face contact for three-dimensional discontinuous deformation analysis. Rock Mech Rock Eng 2004;37(2):95–116.
[28] Wu J-H. Seismic landslide simulations in discontinuous deformation analysis. Comput Geotech 2010;37(5):594–601.
[29] Wu J-H, Lin J-S, Chen C-S. Dynamic discrete analysis of an earthquake-induced large-scale landslide. Int J Rock Mech Min Sci 2009;46(2):397–407.
[30] Chen G. Numerical modeling of rock fall using extended DDA. Chin J Rock Mech Eng 2003;22(6):926–31.
[31] Ma G, Matsuyama H, Nishiyama S, Ohnishi Y. Practical studies on rockfall simulation by DDA. J Rock Mech Geotech Eng 2011;3(1):57–63.
[32] Wu JH, Ohnishi Y, Nishiyama S. A development of the discontinuous deformation analysis for rock fall analysis. Int J Numer Anal Meth Geomech 2005;29(10):971–88.
[33] Beyabanaki SAR, Bagtzoglou AC. Three-dimensional discontinuous deformation analysis (3-D DDA) method for particulate media applications. Geomech Geoeng 2012;7(4):239–53.
[34] Beyabanaki SAR, Bagtzoglou AC. Sphere-boundary edge and sphere-boundary corner contacts model in DDA for simulating particulate media in 3-D. Geomech Geoeng 2014;10(2):1–12.
[35] Beyabanaki SAR, Mikola RG, Hatami K. Three-dimensional discontinuous deformation analysis (3-D DDA) using a new contact resolution algorithm. Comput Geotech 2008;35(3):346–56.
[36] Shi GH. Basic theory of two dimensional and three dimensional contacts. In: Frontiers of discontinuous numerical methods and practical simulations in engineering and disaster prevention. CRC Press; 2013. p. 3–14.
[37] Shi GH. Contact theory. Sci China Technol Sci 2015;58(9):1–47.
[38] Wu JH, Juang C, Lin HM. Vertex-to-face contact searching algorithm for three-dimensional frictionless contact problems. Int J Numer Meth Eng 2005;63(6):876–97.
[39] Yeung M, Jiang Q, Sun N. A model of edge-to-edge contact for three-dimensional discontinuous deformation analysis. Comput Geotech 2007;34(3):175–86.
[40] Zhang H, Liu SG, Zheng L, Zhong GH, Lou S, Wu YQ, et al. Extensions of edge-to-edge contact model in three-dimensional discontinuous deformation analysis for friction analysis. Comput Geotech 2016;71:261–75.
[41] Zhang H, Liu SG, Han Z, Zheng L, Zhang YB, Wu YQ, et al. A new algorithm to identify contact types between arbitrarily shaped polyhedral blocks for three-dimensional discontinuous deformation analysis. Comput Geotech 2016;80:1–15.

[42] Zhang H, Liu SG, Chen GQ, Zheng L, Zhang YB, Wu YQ, et al. Extension of three-dimensional discontinuous deformation analysis to frictional-cohesive materials. Int J Rock Mech Min 2016;86:65–79.
[43] Bakun-Mazor D, Hatzor Y, Glaser S. 3D DDA vs. analytical solutions for dynamic sliding of a tetrahedral wedge. In: 9th international conference on analysis of discontinuous deformation. Singapore: ICADD9; 2009.
[44] Mikola RG, Sitar N. Explicit three dimensional discontinuous deformation analysis for blocky system. In: Proceedings of the 47th US rock mechanics/geomechanics symposium, San Francisco, 23–26 June 2013.
[45] Wu J-H, Ohnishi Y, Shi G-H, Nishiyama S. Theory of three-dimensional discontinuous deformation analysis and its application to a slope toppling at Amatoribashi, Japan. Int J Geomech 2005;5(3):179–95.
[46] Keneti A, Jafari A. Determination of volume and centroid of irregular blocks by a simplex integration approach for use in discontinuous numerical methods. Geomech Geoeng: Int J 2008;3(1):79–84.
[47] Wu J-H. Compatible algorithm for integrations on a block domain of any shape for three-dimensional discontinuous deformation analysis. Comput Geotech 2010;37(1–2):153–63.
[48] Zheng L, Chen G, Li Y, Zhang Y, Kasama K. The slope modeling method with GIS support for rockfall analysis using 3D DDA. Geomech Geoeng 2014;9(2):142–52.